Chemical Engineering Journal 432 (2022) 134433

Contents lists available at ScienceDirect

Chemical Engineering Journal

journal homepage: www.elsevier.com/locate/cej

Collaborative pore partition and pore surface fluorination within a metal–organic framework for high-performance C_2H_2/CO_2 separation

Xing-Ping Fu [a,d], Yu-Ling Wang [a,*], Xue-Feng Zhang [a], Rajamani Krishna [c], Chun-Ting He [a], Qing-Yan Liu [a,*], Banglin Chen [b,*]

[a] College of Chemistry and Chemical Engineering, Key Laboratory of Functional Small Molecules for Ministry of Education, Jiangxi Normal University, Nanchang 330022, Jiangxi, PR China
[b] Department of Chemistry, University of Texas at San Antonio One UTSA Circle, San Antonio, TX 78249-0698, USA
[c] Van 't Hoff Institute for Molecular Sciences, University of Amsterdam, Science Park 904, 1098 XH Amsterdam, The Netherlands
[d] Department of Ecological and Resources Engineering, Fujian Key Laboratory of Eco-industrial Green Technology, Wuyi University, Wuyishan 354300, Fujian, PR China

ARTICLE INFO

Keywords:
Metal-organic frameworks (MOFs)
Adsorption separation
Fluorine substitution effect
Pore-space-partition
Acetylene/carbon dioxide separation
Relationship between structure and property

ABSTRACT

Inspired by the unique properties of fluorous compounds, the deliberate replacement of H atoms with F atoms in organic linkers of metal–organic frameworks (MOFs) could be of highly interesting. Herein we rationally developed a fluorinated MOF of JXNU-12(F) derived from the parent MOF of JXNU-12 in the presence of the pore partition agent. Remarkably, H/F substitution maintains the crystal structures of MOFs but dramatically enhances the C_2H_2/CO_2 separation properties. The C_2H_2 uptake of JXNU-12(F) (298 K and 1 bar) is 1.48 times higher than that of JXNU-12 even though the pore volume of JXNU-12(F) is 84% of JXNU-12. Whereas both MOFs exhibit the same CO_2 uptakes under the same conditions. The C_2H_2/CO_2 adsorption selectivity of JXNU-12 (F) at 1 bar and 298 K is 2 times that of JXNU-12, emphasizing the importance of fluorine substitution. An excellent C_2H_2/CO_2 separation with a large C_2H_2 captured amount of 4.7 mmol g^{-1} was achieved with JXNU-12 (F), ranking among the best-performing MOFs. The significant performance enhancement in JXNU-12(F) is rationalized by the large electronegativity and polarizability of fluorine groups exposed on the pore surfaces and the well-matched pore spaces generated by pore partition for trapping C_2H_2, which collaboratively enhance framework-C_2H_2 interactions as revealed by computional simulations.

1. Introduction

Acetylene (C_2H_2), which is the simplest and important alkyne, is widely utilized for welding and as the raw material for a great number of fine chemicals including synthetic rubber, acetylenic alcohols, and vinyl derivatives [1]. It has been reported that the global acetylene gas market is expected to be 11.42 billion US$ in 2023 [2]. Acetylene can be produced by a oxidative coupling of methane or steam cracking of oil in petrochemical industry [3], leading to a major impurity of carbon dioxide (CO_2) in products. Current technology for purification of C_2H_2 from the gas products is solvent extraction. The utilization of a large amount of organic solvent in the extraction processe generates serious problems of environmental pollution and huge energy consumption. Metal-organic frameworks (MOFs) have emerged as a kind of novel porous solid materials featuring crystalline structures and tunable pore environment [4–7]. MOFs have been shown to be highly promising porous materials for gas separation through physisorptive separation [8–13]. However, C_2H_2 and CO_2 with linear molecular shapes and similar molecular sizes (C_2H_2, 3.32 × 3.34 × 5.7 Å^3; CO_2, 3.18 × 3.33 × 5.36 Å^3) as well as the same kinetic diameter of 3.3 Å (Table S1, supporting information) [14,15] make C_2H_2/CO_2 separation to be an extreme challenge.

The interplay among gas uptake, selectivity and pore volume for an adsorbent is very important for gas separation. A balanced gas uptake, selectivity and pore volume will lead to MOFs for high-performance gas separation. The partition of the channel spaces into suitable pore cages via pore-space-partition strategy not only improves the framework stability but also affords better pore spaces for trapping specific gas molecules [16–18]. The insertion of pore partition agents in MOFs decreases the pore sizes and porosities, but improves gas adsorption through efficient host–guest interactions. Such a strategy is a powerful route for balancing the gas uptake, selectivity and pore volume for MOFs [19,20].

* Corresponding authors.
E-mail addresses: ylwang@jxnu.edu.cn (Y.-L. Wang), qyliuchem@jxnu.edu.cn (Q.-Y. Liu), banglin.chen@utsa.edu (B. Chen).

https://doi.org/10.1016/j.cej.2021.134433
Received 20 November 2021; Received in revised form 25 December 2021; Accepted 28 December 2021
Available online 3 January 2022

On the other hand, the modifying organic ligand with Lewis base sites such as oxygen and nitrogen in MOFs or incorporating inorganic MF_6^{2-} (M = Si and Ti etc.) groups into MOFs is a feasible approach to improve the binding affinity toward C_2H_2 possessing the acidic alkynyl hydrogen atoms [21–24]. However, such Lewis base sites are generally the undesirable binding sites for CO_2 with two electronegative O atoms. Therefore, such a chemical modification approach has resulted in the high-efficient C_2H_2/CO_2 separation [25–27].

Fluorine substituent effects on the organic molecules are well demonstrated [28–32]. The fluorination of organic molecules leads to dramatic changes in physico-chemical properties, imparting to the resultant fluorinated compounds with improvements in hydrophobicity, thermal/chemical stability, lipophobicity, and biological activity [33–35]. The replacing H atoms with F atoms in organic ligands of MOFs is expected to be of great interest. Due to the entirely different electronegativity and polarizability between H and F atoms, fluorine substitution in MOFs may trigger impactful changes in physico-chemical properties of MOFs. A few of fluorinated MOFs have been demonstrated with interesting gas adsorption properties including H_2, CO_2 and fluorocarbons adsorption [36–41]. Unfortunately, the lack of corresponding nonfluorinated MOFs or the F group as an innocent group during the adsorption process hinders the direct comparison of gas adsorption properties between fluorinated and nonfluorinated MOFs [42–46]. Thus the systematic and in-depth comparative studies of gas adsorption/separation properties for the pair of fluorinated and nonfluorinated MOFs are urgently needed.

Here we report a pair of MOFs with the pore partition agent of 2,4,6-tri(4-pyridinyl)-1,3,5-triazine (tpt), $\{[(CH_3)_2NH_2]_2[Ni_3(\mu_3\text{-}O)(BPDC)_3(tpt)]\}_n$ (named JXNU-12) based on biphenyl-4,4′-dicarboxylic ($BPDC^{2-}$) ligand and $\{[(CH_3)_2NH_2]_2[Ni_3(\mu_3\text{-}O)(TFBPDC)_3(tpt)]\}_n$ (coined JXNU-12(F)) based on 3,3′,5,5′-tetrakis(fluoro)biphenyl-4,4′-dicarboxylic ($TFBPDC^{2-}$) ligand. Thanks to great tunability of the structural modules of MOFs [47,48], JXNU-12(F) was readily obtained using the H_2-TFBPDC ligand derived from partial fluorination of H_2-BPDC ligand. Benefitting from the most similar van der Waal's radii and the closest steric sizes between H and F atoms, fluorination achieves the isomorphic JXNU-12 and JXNU-12(F), which provide the elegant examples for in-depth comparative studies of C_2H_2/CO_2 separation performance for the pair of fluorinated and nonfluorinated MOFs. Remarkably, the fluorination dramatically increases the C_2H_2 sorption capacity whereas the CO_2 uptake capacities for both MOFs are almost unchanged, considerably enhancing C_2H_2/CO_2 separation performance for JXNU-12(F). Thus the pore partition and the installation of fluorine groups on the pore surfaces fine-tune the pore microenvironments elaborately, which collaboratively endow JXNU-12(F) with the optimized pore spaces for accommodating C_2H_2.

2. Experimental section

2.1. Synthesis of JXNU-12

A mixture of $Ni(NO_3)_2{\cdot}6H_2O$ (11.6 mg, 0.04 mmol), biphenyl-4,4'-dicarboxylate acid (12.6 mg, 0.04 mmol), 2,4,6-tri(4-pyridyl)-1,3,5-triazine (4.8 mg, 0.015 mmol), DMF (2 mL), and HBF_4 (0.03 mL) was sealed in a 20 mL vial and heated at 110 °C for 2 days, After cooling to room temperature, the greenish hexagonal prisms-shaped crystals were obtained after washed with DMF (yield 62%, based on $Ni(NO_3)_2{\cdot}6H_2O$.

2.2. Synthesis of JXNU-12(F)

A mixture of $Ni(NO_3)_2{\cdot}6H_2O$ (11.6 mg, 0.04 mmol), 3,3',5,5'-tetrakis(fluoro)biphenyl-4,4'-dicarboxylate acid (12.6 mg, 0.04 mmol), 2,4,6-tri(4-pyridyl)-1,3,5-triazine (4.8 mg, 0.015 mmol), DMF (2 mL), and HBF_4 (0.12 mL) was sealed in a 20 mL vial and heated at 110 °C for 2 days, After cooling to room temperature, the pale greenish strip-shaped crystals were obtained after washed with DMF (yield 69 %, based on $Ni(NO_3)_2{\cdot}6H_2O$.

2.3. Characterizations

The powder X-ray diffraction patterns (PXRD) were recorded on a Rigaku DMAX 2500 powder diffractometer using Cu-Kα (λ = 1.54056 Å). Single-crystal X-ray diffraction experiments were carried out with a Rigaku Oxford SuperNova diffractometer (Mo-Kα radiation, λ = 0.71073 Å). The detailed crystal refinement information is provided in supporting information.

Gas sorption–desorption isotherms were measured on a Micromeritics ASAP 2020 HD88 surface-area analyzer. Transient breakthrough simulations were carried out with 50/50 C_2H_2/CO_2 mixtures in adsorption columns using the methodology described previously [45]. The detailed breakthrough experiments for separation of C_2H_2/CO_2 mixtures are provided in supporting information.

3. Results and discussion

3.1. Crystal structure

Initially, the parent MOF of JXNU-12 was synthesized from $Ni(NO_3)_2{\cdot}6H_2O$, H_2-BPDC and tpt in DMF solvent in the presence of HBF_4. Based on the molecular design approach, the utilization of partly fluorinated H_2-TFBPDC analogue in the similar reaction afforded the fluorinated JXNU-12(F). Single-crystal X-ray diffraction revealed that JXNU-12 and JXNU-12(F) are isomorphic (Table S2 and Fig. S1). The anionic $[Ni_3(\mu_3\text{-}O)(BPDC)_3(tpt)]^{2-}$ or $[Ni_3(\mu_3\text{-}O)(TFBPDC)_3(tpt)]^{2-}$ framework is charge-balanced by the extraframework $(CH_3)_2NH_2^+$ ions derived from decomposition of DMF solvents. The present three-dimensional (3D) frameworks constructed from trimeric $[Ni_3(\mu_3\text{-}O)]$ culsters can be described as the variants of the MIL-88 type framework installed with the pore partition agent of tpt (Fig. 1a) [49,50]. As depicted in Fig. 1b and 1c, each planar $[Ni_3(\mu_3\text{-}O)]$ unit is linked by six dicarboxylate ligands and three tpt ligands to give a 3D framework (Fig. S2). The use of the pore partition agent of tpt has resulted in the cylindrical cages and trigonal bipyramidal cages. Each cylindrical cage is formed from six $[Ni_3(\mu_3\text{-}O)]$ units, six dicarboxylate ligands and two tpt ligands (Fig. 1d and 1e). Each trigonal bipyramidal cage is built from five $[Ni_3(\mu_3\text{-}O)]$ units, six dicarboxylate ligands and three tpt ligands (Fig. 1f and 1 g). Owing to the electrostatic repulsion between F atoms and carboxylate O atoms in the $TFBPDC^{2-}$ ligand, the large torsion angles between benzene planes and their attached carboxylate planes (56.4° and 57.8°) are generated (Fig. S1b). In contrast, the benzene planes with their attached carboxylate planes are nearly coplanar in $BPDC^{2-}$ ligand. As a result, some F atoms of $TFBPDC^{2-}$ in JXNU-12(F) point toward the interior of trigonal bipyramidal cages, which narrows down the pore sizes (from 14 Å to 10.6 Å) and provides the highly polarized and fluorophilic pore cage environments (Fig. 1g). Since the F atoms are located on the shell of the cylindrical cage in JXNU-12(F), the reduced window sizes for the cylindrical cage are observed (Fig. 1e). Such an arrangment of the F groups in the cylindrical cage makes fluorine functionalization of the pore walls. Calculation by PLATON software revealed that the solvent accessible voids for JXNU-12 and JXNU-12(F) are 65.7% and 60.3% of the unit cell volumes, respectively. The guest solvents in JXNU-12 and JXNU-12(F) can be exchanged with acetonitrile, which was easy removed from the 3D frameworks by heating and vacuum (Fig. S3). The phase purity of the compounds was evidenced by the powder X-ray diffraction patterns (PXRD) (Fig. S4). After exposure to air under ambient conditions for a month or soaked in water for 10 h, JXNU-12(F) maintains the framework integrity and crystallinity (Fig. S4), while JXNU-12 lost its crystallinity. Such phenomena indicate the chemical stability of the fluorinated JXNU-12(F) is greatly improved in comparison with JXNU-12, suggesting the substitution of H atoms with F atoms in the organic ligands improves the chemical stability of the fluorinated MOF. Furthermore, the water

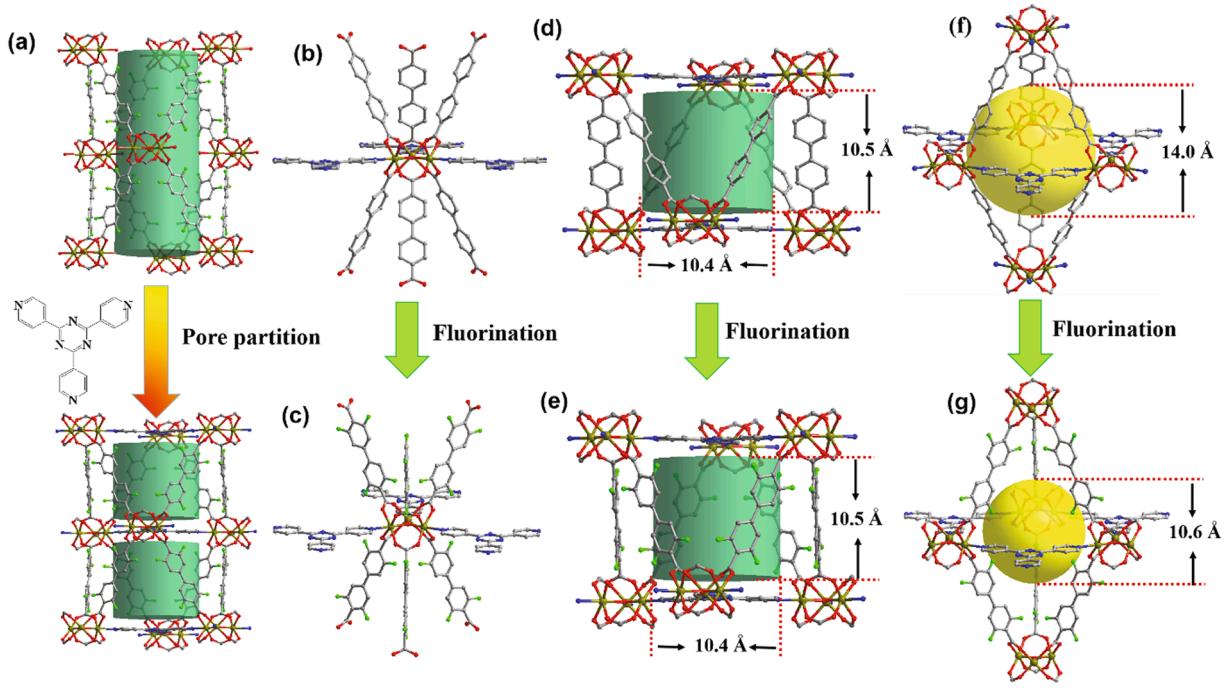

Fig. 1. (a) One-dimensional channel in MIL-88 type framework is divided into small cages by insertion of the pore partition agent of tpt. (b) and (c) [$Ni_3(\mu_3\text{-}O)(COO)_6$] units, (d) and (e) cylindrical cages, (f) and (g) trigonal bipyramidal cages in JXNU-12 and JXNU-12(F).

contact angle for JXNU-12 (26.4°) is much smaller than that of JXNU-12 (F) (41.5°) (Fig. S5), suggesting that the introduction of fluorine atoms into the organic linkers significantly enhances the hydrophobicity of the MOF material.

3.2. Gas adsorption and separation performance

Nitrogen sorption isotherms at 77 K were performed on JXNU-12 and JXNU-12(F) to experimentally examine their permanent porosities. Both MOFs showed typically reversible type-I isotherms, indicating their microporous structures. The maximum N_2 adsorption capacities are 667 and 565 $cm^3\ g^{-1}$ for JXNU-12 and JXNU-12(F), respectively (Fig. 2a). The Brunauer-Emmett-Teller (BET) and Langmuir surface areas were 2544 and 2882 $m^2\ g^{-1}$ for JXNU-12 and 2154 and 2431 $m^2\ g^{-1}$ for JXNU-12(F), respectively (Fig. S6 and Table 1). The total pore volumes estimated from the N_2 uptakes for JXNU-12 and JXNU-12(F) are 1.03 and 0.86 $cm^3\ g^{-1}$, in agreement with the theoretical value of 1.02 and 0.81 $cm^3\ g^{-1}$. The experimental pore volumes for both MOFs are slightly higher than their theoretical values, which could be resulted from the crystal defects induced by the acid modulator in the reactions [51]. The

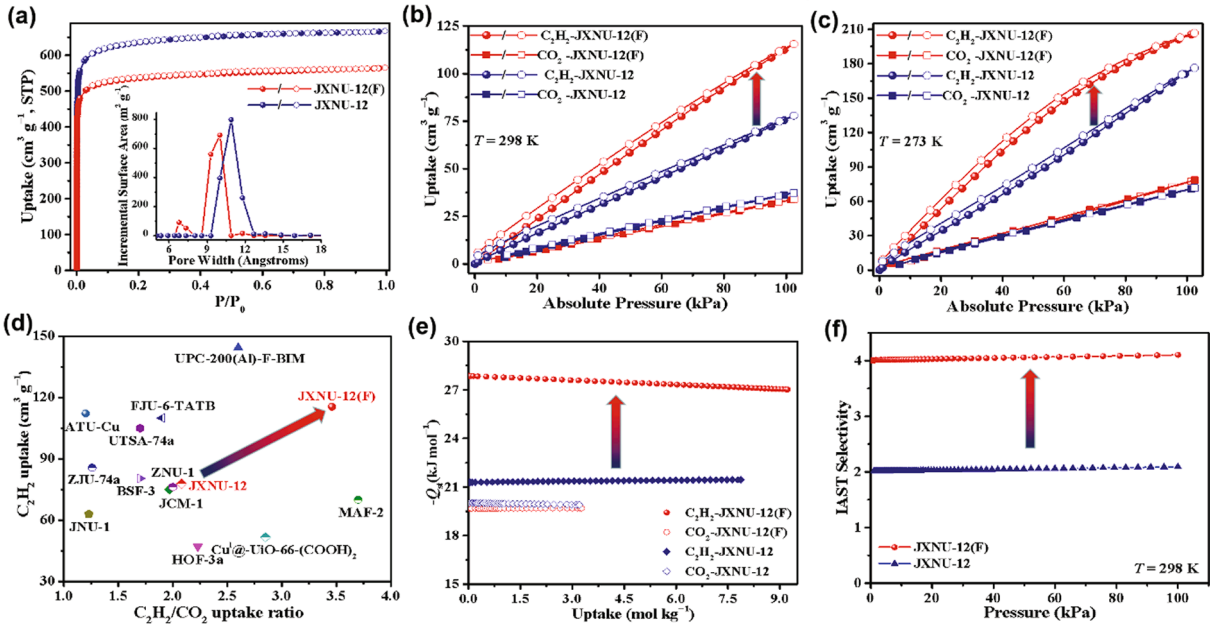

Fig. 2. (a) 77 K N_2 adsorption isotherms and pore size distribution for JXNU-12 and JXNU-12(F) (Inset). (b and c) C_2H_2 and CO_2 adsorption isotherms of JXNU-12 and JXNU-12(F). (d) Comparison of MOFs with top-high C_2H_2 uptake and C_2H_2/CO_2 uptake ratio at 298 K and 1 bar. (e) The Q_{st} and (f) IAST selectivity for JXNU-12 and JXNU-12(F).

Table 1
Comparison of surface area, total pore volume, gas uptake (298 K and 1 bar), IAST selectivity (C_2H_2/CO_2 50:50, at 1 bar and 298 K), and CO_2/C_2H_2 (50/50) breakthrough performance with a gas flow rate of 2.0 mL min^{-1} at 298 K.

	S_{BET} (m^2 g^{-1})	total pore volumes (cm^3 g^{-1})	C_2H_2 uptake (cm^3 g^{-1})	CO_2 uptake (cm^3 g^{-1})	S_{ads}	C_2H_2 breakthrough time (min g^{-1})	Interval time between C_2H_2 and CO_2 breakthrough (min g^{-1})	The C_2H_2-capture amount (mmol g^{-1})
JXNU-12	2544	1.03	77.9	37.3	2.0	78	30	3.1
JXNU-12 (F)	2154	0.86	115.5	33.4	4.1	117	70	4.7

main pore size distribution reduces from 10.9 Å for JXNU-12 to 10.0 Å for JXNU-12(F) (Fig. 2a (inset)). The results indicate the incorporation of fluorine atoms into the organic linkers led to an obvious decrease on the porosity, surface area and pore volume, and a slight decrease of pore aperture, in consistent with the results of crystal structures. Compared to those of JXNU-12, the decrease in porosity, surface area and pore volume for JXNU-12(F) mainly arise from increase of the relatively larger inherent steric hindrance of F atoms and its molecular weight.

To explore the possibility of tuning the C_2H_2 and CO_2 sorption performance via fluorine substitution. The single-component isotherms of C_2H_2 and CO_2 for JXNU-12 and JXNU-12(F) were collected. The results showed the C_2H_2 uptakes for both MOFs are obviously higher than CO_2 uptakes under the same conditions (Fig. 2b, 2c and Fig. S7). JXNU-12 takes up 77.9 cm^3 g^{-1} of C_2H_2 and 37.3 cm^3 g^{-1} of CO_2 under 298 K and 1 bar (Fig. 2b). JXNU-12 shows distinct C_2H_2 and CO_2 sorption amounts with the uptake ratios of 2.08 at 298 K and 1 bar, which is higher than those of noted MOFs including FJU-90a (1.75) [19], SIFSIX-Cu-TPA (1.7) [21], BSF-3 (1.7) [52], SNNU-45 (1.38) [53], and NKMOF-1-Ni (1.19) [54]. Remarkably, JXNU-12(F) adsorbs much more C_2H_2 than that of JXNU-12 under the same conditions in the full pressure region (Fig. 2b, 2c and Fig. S7). The C_2H_2 uptake (115.5 cm^3 g^{-1}) for JXNU-12(F) is considerably higher by 1.48 times than that of JXNU-12 at 298 K and 1 bar, contradictory to the order of surface areas. Such marked difference on C_2H_2 sorption between JXNU-12 and JXNU-12(F) indicates a significantly enhanced C_2H_2 uptake was achieved by fluorine substitution. The incorporation of the F groups into JXNU-12(F) leads to the reduced pore sizes and pore apertures, but facilitates more closer contacts betwen C_2H_2 and pore walls. Thus the shrunken and highly fluorophilic pore spaces induced by pore partition and fluorination in JXNU-12(F) are well-matched for trapping C_2H_2. Moreover, no loss of the C_2H_2 uptake for JXNU-12(F) was observed in the recycling measurements (Fig. S8), suggesting an excellent sorption recyclability for JXNU-12(F). Even more surprising is that JXNU-12 and JXNU-12(F) exhibit almost the same CO_2 sorption amounts under same conditions, as evidenced by the overlapped sorption isotherms (Fig. 2b, 2c and Fig. S7). It is noteworthy that JXNU-12 has the larger surface area than that of JXNU-12(F). As a result, the CO_2 uptake per unit surface area for JXNU-12(F) is much lower than that of JXNU-12 under same conditions, suggesting the highly fluorophilic pore environments are adverse for capturing CO_2. Fluorination thus can remarkably increase C_2H_2 sorption capacity. The substantial increase of the C_2H_2/CO_2 uptake ratios are achieved for JXNU-12(F) with the C_2H_2/CO_2 uptake ratio of 3.46 at 298 K and 1 bar, which is higher than that of 2.08 for JXNU-12 and ranks among the benchmark MOFs including UPC-200(Al)-F-BIM (2.6) [55], JNU-1 (1.23) [56], and ATC-Cu (1.2) [57] (Fig. 2d). The fluorination achieved JXNU-12(F) shows the strong binding sites for C_2H_2 and weaker binding affinity to CO_2, which enables JXNU-12(F) highly promising potential for discriminating C_2H_2 and CO_2 gases.

A notable increase of C_2H_2 adsorption enthalpy (Q_{st}) was indeed observed from 21.3 kJ mol^{-1} for JXNU-12 to 28.0 kJ mol^{-1} for JXNU-12 (F) at zero-loading (Fig. 2e and Fig. S9), reflecting stronger affinity toward C_2H_2 of JXNU-12(F) than that of JXNU-12. The much different Q_{st} values mean the displacement of H with F is feasible for tuning the interactions between C_2H_2 and framework. The Q_{st} of CO_2 for JXNU-12(F) (19.7 kJ mol^{-1}) and JXNU-12 (19.9 kJ mol^{-1}) are almost the same. The Q_{st} values of C_2H_2 are much larger than those of CO_2 further enable JXNU-12(F) with the ability for discriminating C_2H_2 and CO_2 gases, facilitating an excellent C_2H_2/CO_2 separation performance. Furthermore, the ideal adsorbed solution theory (IAST) calculation was utilized to estimate the adsorptive selectivity (S_{ads}) of C_2H_2/CO_2 (50/50) mixtures. As shown in Fig. 2f, JXNU-12 shows the C_2H_2/CO_2 selectivity of 2.0 at 298 K, while JXNU-12(F) exhibits a notably enhanced C_2H_2/CO_2 selectivity of 4.1. Although the selectivity value of C_2H_2/CO_2 for JXNU-12(F) is lower than the recorded IAST selectivity of UTSA-300a (7 4 3) [23] and CPL-1-NH_2 (1 1 9) [58] having the molecular sieve effect, but is comparable to those of benchmark MOFs of FJU-90 (4.3) [19], UPC-200 (Fe)-F-H_2O (2.25) [55] and FJU-6-TATB (3.1) [59]. The C_2H_2/CO_2 selectivity of JXNU-12(F) at 1 bar is 2 times that of JXNU-12, emphasizing the importance of fluorine substitution. Therefore, the introduction of the F groups into MOF exerts a pronounced impact on C_2H_2 uptake and C_2H_2/CO_2 selectivity. As a result, the large C_2H_2 uptake, large pore volume and moderate selectivity render JXUN-12(F) highly promising for C_2H_2/CO_2 separation.

3.3. Breakthrough performance

Transient breakthrough simulations were performed with the C_2H_2/CO_2 (50/50) mixtures under 298 K and 1 bar [60,61]. As shown in Fig. 3a, the dimensionless τ_{break} value of C_2H_2 for JXNU-12(F) is much larger than that of JXNU-12. The τ_{break} interval between C_2H_2 and CO_2 for JXNU-12(F) is significantly larger than that of JXNU-12, further emphasizing the importance of fluorine substitution. The separation potential (ΔQ) [61] calculated from breakthrough simulation curves for JXNU-12(F) is notably larger than that of JXNU-12 and those of leading MOFs such as Cu^I@UiO-66-$(COOH)_2$ [4], CPL-1-NH_2 [58], and MUF-17 [62] (Fig. 3b). Furthermore, the practical breakthrough experiments for C_2H_2/CO_2 (50/50) mixtures were flowed over packed columns of JXNU-12(F) and JXNU-12 for evaluating their actual dynamic separation performance. As shown in Fig. 3c, C_2H_2/CO_2 mixtures were effectively separated through the fixed bed. As predicted, CO_2 was first detected at the outlet gas, whereas C_2H_2 was preferentially adsorbed by JXNU-12(F) and JXNU-12. For JXNU-12(F), C_2H_2 gas broke through the column after 117 min g^{-1} with a gas flow rate of 2.0 mL min^{-1} at 298 K. The breakthrough time for C_2H_2 surpasses those of some top-performing MOFs, such as SUNN-45 (113 min g^{-1}) [53] and ZJU-74a (81 min g^{-1}) [63]. The breakthrough interval between C_2H_2 and CO_2 reaches 70 min g^{-1}, which is comparable to those of benchmark MOFs of SIFSIX-Cu-TPA (69 min g^{-1}) [21], and SNNU-45 (79 min g^{-1}) [53], but superior to those of prominent MOFs including JNU-1 (34 min g^{-1}) [56], FeNi-M'MOF (29 min g^{-1}) [64], and CPL-1-NH_2 (29 min g^{-1}) [58]. The captured amount for C_2H_2 during the $0 \sim \tau_{break}$ time under the dynamic conditions is 4.7 mmol g^{-1} at 298 K, which outperforms all other top-performing MOFs including ZJU-74a (3.64 mmol g^{-1}) [63], SNNU-45 (3.5 mmol g^{-1}) [53], JCM-1(2.2 mmol g^{-1}) [65], and UTSA-74a (2.46 mmol g^{-1}) [66] (Fig. S10). As shown in Fig. 3c, CO_2 breakthrough times for JXNU-12(F) and JXNU-12 are similar, in line with the results of single-component CO_2 sorption. In contrast, much different in C_2H_2 breakthrough times for JXNU-12(F) and JXNU-12 were obtained. The breakthrough interval between C_2H_2 and CO_2 for JXNU-12 (30 min g^{-1}) is fewer than half of JXNU-12(F), consolidating the higher

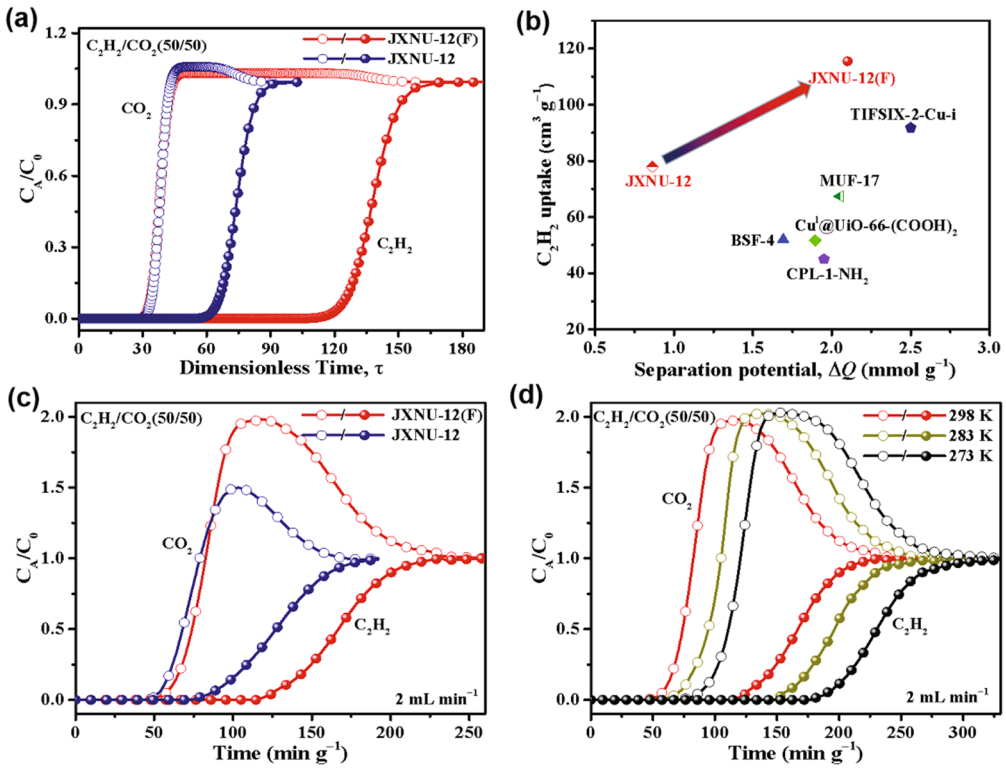

Fig. 3. (a) Breakthrough simulations curves of JXNU-12(F) and JXNU-12 for C_2H_2/CO_2 at 298 K and 1 bar. (b) Comparison of the separation potential and C_2H_2 uptake at 298 K and 1 bar for top-performing MOFs. (c) Experimental breakthrough curves of JXNU-12(F) and JXNU-12 at 298 K and 1 bar. (d) Breakthrough curves of JXNU-12(F) at different temperatures under 1 bar.

separation performace for JXNU-12(F). In addition, both MOFs display the roll-up phenomenon of CO_2 gas, which means the CO_2 molecules adsorbed in the bed can be replaced with the newly entered C_2H_2 molecules. In comparison with JXNU-12, more evident roll-up phenomenon of CO_2 for JXNU-12(F) further indicates JXNU-12(F) has lower binding affinity to CO_2. Finally, we performed dynamic column breakthrough experiments at different temperatures and gas flow rates for JXNU-12 (F).

It is noted that the breakthrough times of C_2H_2 reach 150 min g^{-1} at 283 K and even 181 min g^{-1} at 273 K with a total flow of 2 mL min^{-1} (Fig. 3d). When the gas flow rate was 8 mL min^{-1} at 298 K, JXNU-12(F) still displays a good separation performance with C_2H_2 breakthrough time reach 36 min g^{-1} (Fig. S11). Benefitting from the relatively low C_2H_2 adsorption enthalpy, JXNU-12(F) was readily regenerated under ambeint pressure by simply flushing the adsorption column with helium gas at 298 K. As shown in the desorption curves (Fig. S12), most of adsorbed CO_2 were removed within 5 min under the continuing purge of He flow. By contrast, the desorption of C_2H_2 was much slower. Finally, almost the same retention times for C_2H_2 and CO_2 were obtained after five column breakthrough cycles (Fig. S13), indicating good

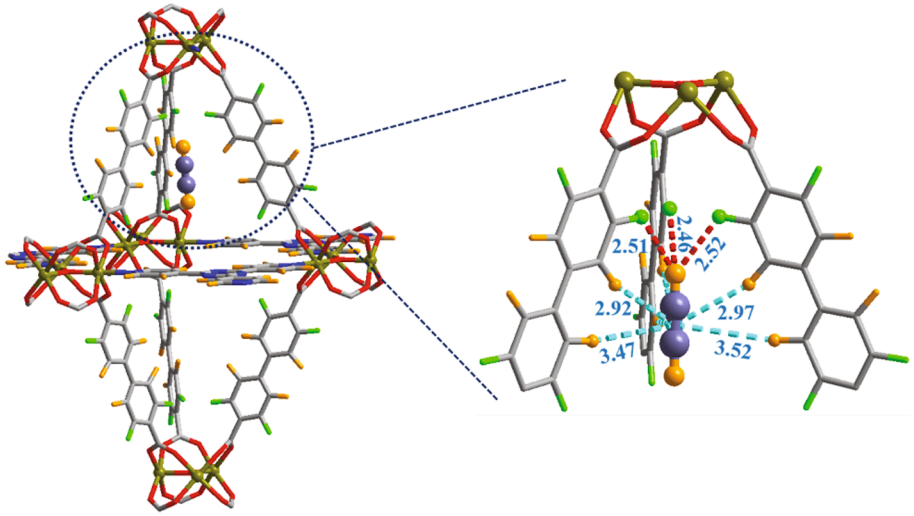

Fig. 4. The preferential C_2H_2 adsorption site calculated from GCMC simulation for JXNU-12(F). Element key: Ni (dark yellow), C (gray), F (bright green), O (red) and H (bright orange) in JXNU-12(F); C (blue gray) and H (bright orange) in C_2H_2. The labeled distance is measured in Å. (For interpretation of the references to colour in this figure legend, the reader is referred to the web version of this article.)

recyclability for JXNU-12(F). Overall, the dynamic experiments demonstrated JXNU-12(F) is capable of separating C_2H_2 and CO_2 gases effificently and ranks among the best-performing MOFs.

3.4. Separation mechanism

To in-depth gain the microscopic insights into C_2H_2/CO_2 separation mechanism induced by fluorine substitution, we performed grand ganonical Monte Carlo (GCMC) simulations on JXNU-12(F). As shown in Fig. 4, the preferential binding site for C_2H_2 molecule was found to be located in the top of a trigonal bipyramidal cage. C_2H_2 trapped in a trigonal bipyramidal cage is closely surrounded by three $TFBPDC^{2-}$ ligands with three F atoms pointing toward the interior wall of cage. C_2H_2 is found to be interacted with the strong electronegative F atoms. Three F atoms of three $TFBPDC^{2-}$ ligands simultaneously interact with a C_2H_2 molecule, resulting in strong C − H···F hydrogen bonds with close H···F of 2.46, 2.51, and 2.52 Å, which are much shorter than the van der Waals contact distance (2.65 Å) between H and F atoms, generating the substantial contacts between them. Furthermore, six C–H (benzene)···π interactions with the C≡C group of C_2H_2 with H···π distances from 2.9 to 3.5 Å were observed. The multiple interactions synergistically bind a C_2H_2 molecule, facilitating the strong C_2H_2-framework interactions. Thus the encapsulation of the pore partition agent and F groups into MOFs affords the highly suitable micropore environments to match C_2H_2. The large electronegative F atoms of the organic linkers dominate the host–guest interactions between the adsorbent and adsorbate, boosting the sorption of C_2H_2 over CO_2.

4. Conclusion

In conclusion, we have discovered a fluorinated MOF of JXNU-12(F) derived from the parent MOF of JXNU-12 with the pore partition agent. The fluorination successfully achieves the isomorphous JXNU-12 and JXNU-12(F), accompanied by the significant changes in C_2H_2 sorption amount and C_2H_2/CO_2 separation properties. The foregoing results showed that JXNU-12(F) exhibits considerably higher C_2H_2 uptake and C_2H_2/CO_2 adsorption selectivity than those of JXNU-12. JXNU-12(F) displays strong binding affinity toward C_2H_2 but weaker binding sites for CO_2 as induced by fluorine substitution and pore partition collaboratively. The significant performance improvement in JXNU-12(F) is ascribed to the well-matched pore spaces induced by pore partition and florination of pore surfaces for trapping C_2H_2 and the enhanced C_2H_2-framework interactions via the formation of strong C − H···F hydrogen bonds, as evidenced by GCMC simulations. The highly efficient C_2H_2/CO_2 separation ability for JXNU-12(F) was clearly demonstrated by breakthrough experiments. In light of the conceptual strategy of fluorine substitution, one can foresee that a continuous succession of gas adsorption/separation properties of MOFs can be elaborately modulated by the H/F substitution.

Declaration of Competing Interest

The authors declare that they have no known competing financial interests or personal relationships that could have appeared to influence the work reported in this paper.

Acknowledgements

This work is financially supported by the National Natural Science Foundation of China (22061022 and 21861020), the Foundation for Academic and Technical Leaders of Major Disciplines of Jiangxi Province (20204BCJL22043), and Jiangxi Provincial Natural Science Foundation (20202ZDB01004).

Appendix A. Supplementary data

Supplementary data to this article can be found online at https://doi.org/10.1016/j.cej.2021.134433.

References

[1] P. Pässler, W. Hefner, K. Buckl, H. Meinass, H.J. Wernicke, G. Ebersberg, R. Müller, J. Bässler, H. Behringer, D. Mayer, Ullmann's encyclopedia of industrial chemistry, Wiley-VCH, Weinheim, Germany, 2008.
[2] Research and Markets, Acetylene Global Market Report 2020. www.researchandmarkets. com (accessed February 2020).
[3] A. Granada, S.B. Karra, S.M. Senkan, Conversion of methane into acetylene and ethylene by the chlorine-catalyzed oxidative-pyrolysis (CCOP) process. 1. Oxidative pyrolysis of chloromethane, Ind. Eng. Chem. Res. 26 (9) (1987) 1901–1905.
[4] L. Zhang, K. Jiang, L.F. Yang, L.B. Li, E.L. Hu, L. Yang, K. Shao, H.B. Xing, Y.J. Cui, Y. Yang, B. Li, B.L. Chen, G.D. Qian, Benchmark C_2H_2/CO_2 Separation in an Ultra-Microporous Metal−Organic Framework via Copper(I)-Alkynyl Chemistry, Angew. Chem. Int. Ed. 60 (2021) 15995−16002.
[5] X.R. Zhang, W.D. Fan, W.F. Jiang, Y. Li, Y.T. Wang, M.Y. Fu, D.F. Sun, Optimizing Fe-based metal-organic frameworks through ligand conformation regulation for efficient dye adsorption and C_2H_2/CO_2 separation, Chem. Eur. J. 27 (2021) 10693–10699.
[6] S.B. Geng, E. Lin, X. Li, W.S. Liu, T. Wang, Z.F. Wang, D. Sensharma, S. Darwish, Y. H. Andaloussi, T. Pham, P. Cheng, M.J. Zaworotko, Y. Chen, Z.J. Zhang, Scalable room-temperature synthesis of highly robust ethane-selective metal−organic frameworks for efficient ethylene purification, J. Am. Chem. Soc. 143 (2021) 8654–8660.
[7] Y. Xue, X.Y. Bai, J. Zhang, Y. Wang, S.N. Li, Y.C. Jiang, M.C. Hu, Q.G. Zhai, Precise pore space partitions combined with high−density hydrogen-bonding acceptors within metal−organic frameworks for highly efficient acetylene storage and separation, Angew. Chem. Int. Ed. 60 (2021) 10122–10128.
[8] Z.Z. Xu, X.H. Xiong, J.B. Xiong, R. Krishna, L.B. Li, Y.L. Fan, F. Luo, B.L. Chen, A robust Th-azole framework for highly efficient purification of C_2H_4 from a $C_2H_4/C_2H_2/C_2H_6$ mixture, Nat. Commun. 11 (2020) 3163.
[9] L.Z. Cai, Z.Z. Yao, S.J. Lin, M.S. Wang, G.C. Guo, Photoinduced electron-transfer (PIET) strategy for selective adsorption of CO_2 over C_2H_2 in a MOF, Angew. Chem. Int. Ed. 133 (2021) 18371–18378.
[10] Z. Shi, Y.u. Tao, J. Wu, C. Zhang, H. He, L. Long, Y. Lee, T. Li, Y.-B. Zhang, Robust metal-triazolate frameworks for CO_2 capture from flue gas, J. Am. Chem. Soc. 142 (6) (2020) 2750–2754.
[11] L. Zhang, K.e. Jiang, J. Zhang, J. Pei, K. Shao, Y. Cui, Y.u. Yang, B. Li, B. Chen, G. Qian, Low-cost and high-performance microporous metal-organic framework for separation of acetylene from carbon dioxide, ACS. Sustain Chem. Eng. 7 (1) (2019) 1667–1672.
[12] W. Fan, X. Wang, X. Liu, B. Xu, X. Zhang, W. Wang, X. Wang, Y. Wang, F. Dai, D. Yuan, D. Sun, Regulating C_2H_2 and CO_2 storage and separation through pore environment modification in a microporous Ni-MOF, ACS. Sustain Chem. Eng. 7 (2) (2019) 2134–2140.
[13] H. Li, L.B. Li, R.-B. Lin, W. Zhou, Z.J. Zhang, S.C. Xiang, B.L. Chen, Porous metal-organic frameworks for gas storage and separation: Status and challenges, Energy Chem. 1 (2019), 100006.
[14] C.R. Reid, K.M. Thomas, Adsorption kinetics and size exclusion properties of probe molecules for the selective porosity in a carbon molecular sieve used for air separation, J. Phys. Chem. B. 105 (2001) 10619–10629.
[15] J.R. Li, R.J. Kuppler, H.C. Zhou, Selective gas adsorption and separation in metal−organic frameworks, Chem. Soc. Rev. 38 (2009) 1477–1504.
[16] Y. Wang, X.X. Jia, H.J. Yang, Y.X. Wang, X.T. Chen, A.N. Hong, J.P. Li, X.H. Bu, P. Y. Feng, A strategy for constructing pore-space-partitioned MOFs with high uptake capacity for C_2 hydrocarbons and CO_2, Angew. Chem. Int. Ed. 59 (2020) 19027–19030.
[17] Y.X. Wang, X. Zhao, H.J. Yang, X.H. Bu, Y. Wang, X.X. Jia, J.P. Li, P.Y. Feng, A tale of two trimers from two different worlds: a COF-inspired synthetic strategy for pore-space partitioning of MOFs, Angew Chem. Int. Ed. 58 (2019) 6316–6320.
[18] S.-T. Zheng, X. Zhao, S. Lau, A. Fuhr, P. Feng, X. Bu, Entrapment of metal clusters in metal-organic framework channels by extended hooks anchored at open metal sites, J. Am. Chem. Soc. 135 (28) (2013) 10270–10273.
[19] Y. Ye, Z. Ma, R.-B. Lin, R. Krishna, W. Zhou, Q. Lin, Z. Zhang, S. Xiang, B. Chen, Pore space partition within a metal-organic framework for highly efficient C_2H_2/CO_2 separation, J. Am. Chem. Soc. 141 (9) (2019) 4130–4136.
[20] H. Yang, Y. Wang, R. Krishna, X. Jia, Y. Wang, A.N. Hong, C. Dang, H.E. Castillo, X. Bu, P. Feng, Pore-space-partition-enabled exceptional ethane uptake and ethane-selective ethane-ethylene separation, J. Am. Chem. Soc. 142 (2020) 2222–2227.
[21] H. Li, C. Liu, C. Chen, Z. Di, D. Yuan, J. Pang, W. Wei, M. Wu, M. Hong, An unprecedented pillar-cage fluorinated hybrid porous framework with highly efficient acetylene storage and separation, Angew. Chem. Int. Ed. 60 (14) (2021) 7547–7552.
[22] Y. Belmabkhout, Z.Q. Zhang, K. Adil, P.M. Bhatt, A. Cadiau, V. Solovyeva, H. B. Xing, M. Eddaoudi, Hydrocarbon recovery using ultra-microporous fluorinated MOF platform with and without uncoordinated metal sites: I- structure properties relationships for C_2H_2/C_2H_4 and CO_2/C_2H_2 separation, Chem. Eng. J. 359 (2019) 32–36.

[23] R.-B. Lin, L. Li, H. Wu, H. Arman, B. Li, R.-G. Lin, W. Zhou, B. Chen, Optimized separation of acetylene from carbon dioxide and ethylene in a microporous material, J. Am. Chem. Soc. 139 (23) (2017) 8022–8028.

[24] K.-J. Chen, H. Scott, D. Madden, T. Pham, A. Kumar, A. Bajpai, M. Lusi, K. Forrest, B. Space, J. Perry, M. Zaworotko, Benchmark C_2H_2/CO_2 and CO_2/C_2H_2 separation by two closely related hybrid ultramicroporous materials, Chem. 1 (5) (2016) 753–765.

[25] S. Mukherjee, D. Sensharma, K.-J. Chen, M.J. Zaworotko, Crystal engineering of porous coordination networks to enable separation of C_2 hydrocarbons, Chem. Commun. 56 (72) (2020) 10419–10441.

[26] X.-P. Fu, Y.-L. Wang, Q.-Y. Liu, Metal–organic frameworks for C_2H_2/CO_2 separation, Dalton Trans. 49 (46) (2020) 16598–16607.

[27] L. Zhang, K.e. Jiang, L. Li, Y.-P. Xia, T.-L. Hu, Y.u. Yang, Y. Cui, B. Li, B. Chen, G. Qian, Efficient separation of C_2H_2 from C_2H_2/CO_2 mixtures in an acid–base resistant metal–organic framework, Chem. Commun. 54 (38) (2018) 4846–4849.

[28] J.A. Gladysz, D.P. Curran, I.T. Horváth (Eds.), Handbook of Fluorous Chemistry, Wiley, 2004.

[29] B.E. Smart, Fluorine substituent effects (on bioactivity), J. Fluor. Chem. 109 (1) (2001) 3–11.

[30] M. Schlosger, D. Michel, About the "physiological size" of fluorine substituents: Comparison of sensorially active compounds with fluorine and methyl substituted analogues, Tetrahedron. 52 (1996) 99–108.

[31] R.E. Banks, B.E. Smart, J.C. Tatlow, Organofluorine chemistry, Plenum Press, New York, 1994.

[32] B.E. Smart, M. Hudlicky, A.E. Pavlath, Chemistry of Organic Fluorine Compounds II, American Chemical Society, Washington, DC. Chapter 6 (1995) 979−1010.

[33] I.T. Horváth, J. Rabái, Facile catalyst separation without water: fluorous biphase hydroformylation of olefins, Science. 266 (1994) 72–75.

[34] T.H. Chen, L. Popov, W. Kaveevivitchai, Y.C. Chuang, Y.S. Chen, O. Daugulis, A. J. Jacobson, O.Š. Miljanić, Fluorocarbon adsorption in hierarchical porous frameworks, Nat. Commun. 5 (2014) 4368–4373.

[35] M. Pagliaro, R. Ciriminna, New fluorinated functional materials, J. Mater. Chem. 15 (2005) 4981–4991.

[36] T.-H. Chen, I. Popov, W. Kaveevivitchai, Y.-C. Chuang, Y.-S. Chen, A.J. Jacobson, O.Š. Miljanić, Mesoporous fluorinated metal−organic frameworks with exceptional adsorption of fluorocarbons and CFCs, Angew. Chem. Int. Ed. 54 (2015) 13902–13906.

[37] C. Wang, D.-D. Zhou, Y.-W. Gan, X.-W. Zhang, Z.-M. Ye, J.-P. Zhang, A partially fluorinated ligand for two super-hydrophobic porous coordination polymers with classic structures and increased porosities, Natl Sci. Rev. 8 (2021) nwaa094.

[38] P. Pachfule, Y.F. Chen, J.W. Jiang, R. Banerjee, Fluorinated metal−organic frameworks: advantageous for higher H_2 and CO_2 adsorption or not, Chem. Eur. J. 18 (2012) 688–694.

[39] P. Pachfule, Y.F. Chen, S.C. Sahoo, J.W. Jiang, R. Banerjee, Structural isomerism and effect of fluorination on gas adsorption in copper-tetrazolate based metal organic frameworks, Chem. Mater. 23 (2011) 2908–2916.

[40] Y.-B. Wu, C. Xiong, Q.-Y. Liu, J.-G. Ma, F. Luo, Y.-L. Wang, Structural evolution from noninterpenetrated to interpenetrated thorium-organic frameworks exhibiting high propyne storage, Inorg. Chem. 60 (2021) 6472–6479.

[41] L. Pan, M.B. Sander, X.Y. Huang, J. Li, M. Smith, E. Bittner, B. Bockrath, J. K. Johnson, Microporous metal organic materials: promising candidates as sorbents for hydrogen storage, J. Am. Chem. Soc. 126 (2004) 1308–1309.

[42] J. Seo, C. Bonneau, R. Matsuda, M. Takata, S. Kitagawa, Soft secondary building unit: dynamic bond rearrangement on multinuclear core of porous coordination polymers in gas media, J. Am. Chem. Soc. 133 (2011) 9005–9013.

[43] C. Yang, U. Kaipa, Q.Z. Mather, X. Wang, V. Nesterov, A.F. Venero, M.A. Omary, Fluorous metal−organic frameworks with superior adsorption and hydrophobic properties toward oil spill cleanup and hydrocarbon storage, J. Am. Chem. Soc. 133 (2011) 18094–18097.

[44] C. Yang, X. Wang, M.A. Omary, Fluorous metal−organic frameworks for high-density gas adsorption, J. Am. Chem. Soc. 129 (2007) 15454–15455.

[45] Z.-T. Lin, Q.-Y. Liu, L. Yang, C.-T. He, L. Li, Y.-L. Wang, Fluorinated biphenyldicarboxylate-based metal−organic framework exhibiting efficient propyne/propylene separation, Inorg. Chem. 59 (2020) 4030–4036.

[46] Z. Zhang, S.B. Peh, R. Krishna, C. Kang, K. Chai, Y. Wang, D. Shi, D. Zhao, Optimal pore chemistry in an ultramicroporous metal−organic framework for benchmark inverse CO_2/C_2H_2 separation, Angew. Chem. Int. Ed. 60 (2021) 17198–17204.

[47] N.L. Rosi, M. Eddaoudi, D.T. Vodak, J. Eckert, M. O'Keeffe, O.M. Yaghi, Hydrogen storage in microporous metal−organic frameworks, Science 300 (2003) 1127–1129.

[48] D.-X. Xue, A.J. Cairns, Y. Belmabkhout, L. Wojtas, Y. Liu, M.H. Alkordi, M. Eddaoudi, Tunable rare-earth fcu-MOFs: a platform for systematic enhancement of CO_2 adsorption energetics and uptake, J. Am. Chem. Soc. 135 (2013) 7660–7667.

[49] P. Horcajada, F. Salles, S. Wuttke, T. Devic, D. Heurtaux, G. Maurin, A. Vimont, M. Daturi, O. David, E. Magnier, N. Stock, Y. Filinchuk, D. Popov, C. Riekel, G. Férey, C. Serre, How Linker's modification controls swelling properties of highly flexible Iron(III) dicarboxylates MIL-88, J. Am. Chem. Soc. 133 (2011) 17839.

[50] X. Zhao, X. Bu, Q.-G. Zhai, H. Tran, P. Feng, Pore space partition by symmetry-matching regulated ligand insertion and dramatic tuning on carbon dioxide uptake, J. Am. Chem. Soc. 137 (4) (2015) 1396–1399.

[51] D. Bara, C. Wilson, M. Mörtel, M.M. Khusniyarov, S. Ling, B. Slater, S. Sproules, R. S. Forgan, Kinetic control of interpenetration in Fe–biphenyl-4,4′–dicarboxylate metal-organic frameworks by coordination and oxidation modulation, J. Am. Chem. Soc. 141 (20) (2019) 8346–8357.

[52] Y. Zhang, J. Hu, R. Krishna, L. Wang, L. Yang, X. Cui, S. Duttwyler, H. Xing, Rational design of microporous MOFs with anionic boron cluster functionality and cooperative dihydrogen binding sites for highly selective capture of acetylene, Angew. Chem. Int. Ed. 59 (40) (2020) 17664–17669.

[53] Y.-P. Li, Y. Wang, Y.-Y. Xue, H.-P. Li, Q.-G. Zhai, S.-N. Li, Y.-C. Jiang, M.-C. Hu, X. Bu, Ultramicroporous building units as a path to bi-microporous metal-organic frameworks with high acetylene storage and separation performance, Angew. Chem. Int. Ed. 58 (38) (2019) 13590–13595.

[54] Y.-L. Peng, T. Pham, P. Li, T. Wang, Y. Chen, K.-J. Chen, K.A. Forrest, B. Space, P. Cheng, M.J. Zaworotko, Z. Zhang, Robust ultramicroporous metal-organic frameworks with benchmark affinity for acetylene, Angew. Chem. Int. Ed. 57 (34) (2018) 10971–10975.

[55] W. Fan, S. Yuan, W. Wang, L. Feng, X. Liu, X. Zhang, X. Wang, Z. Kang, F. Dai, D. Yuan, D. Sun, H.-C. Zhou, Optimizing multivariate metal-organic frameworks for efficient C_2H_2/CO_2 separation, J. Am. Chem. Soc. 142 (19) (2020) 8728–8737.

[56] H. Zeng, M.o. Xie, Y.-L. Huang, Y. Zhao, X.-J. Xie, J.-P. Bai, M.-Y. Wan, R. Krishna, W. Lu, D. Li, Induced fit of C_2H_2 in a flexible MOF through cooperative action of open metal sites, Angew. Chem. Int. Ed. 58 (25) (2019) 8515–8519.

[57] Z. Niu, X. Cui, T. Pham, G. Verma, P.C. Lan, C. Shan, H. Xing, K.A. Forrest, S. Suepaul, B. Space, A. Nafady, A.M. Al-Enizi, S. Ma, A MOF-based ultra-strong acetylene nano-trap for highly efficient C_2H_2/CO_2 separation, Angew. Chem. Int. Ed. 60 (10) (2021) 5283–5288.

[58] L. Yang, L. Yan, Y. Wang, Z. Liu, J. He, Q. Fu, D. Liu, X. Gu, P. Dai, L. Li, X. Zhao, Adsorption site selective occupation strategy within a metal-organic framework for highly efficient sieving acetylene from carbon dioxide, Angew. Chem. Int. Ed. 60 (9) (2021) 4570–4574.

[59] L. Liu, Z. Yao, Y. Ye, Y. Yang, Q. Lin, Z. Zhang, M. O'Keeffe, S. Xiang, Integrating the pillared-layer strategy and pore-space partition method to construct multicomponent MOFs for C_2H_2/CO_2 separation, J. Am. Chem. Soc. 142 (20) (2020) 9258–9266.

[60] R. Krishna, Methodologies for evaluation of metal-organic frameworks in separation applications, RSC Adv. 5 (2015) 52269–52295.

[61] R. Krishna, Screening metal-organic frameworks for mixture separations in fixed-bed adsorbers using a combined selectivity/capacity metric, RSC Adv. 7 (57) (2017) 35724–35737.

[62] O.T. Qazvini, R. Babarao, S.G. Telfer, Multipurpose metal−organic framework for the adsorption of acetylene: ethylene purification and carbon dioxide removal, Chem. Mater. 31 (2019) 4919–4926.

[63] J. Pei, K. Shao, J.X. Wang, H.M. Wen, Y. Yang, Y. Cui, R. Krishna, B. Li, G.D. Qian, A chemically stable hofmann-type metal−organic framework with sandwich-like binding sites for benchmark acetylene capture, Adv. Mater. 32 (2020) 1908275.

[64] J. Gao, X. Qian, R.-B. Lin, R. Krishna, H. Wu, W. Zhou, B. Chen, Mixed metal-organic framework with multiple binding sites for efficient C_2H_2/CO_2 separation, Angew. Chem. Int. Ed. 59 (11) (2020) 4396–4400.

[65] J. Lee, C.Y. Chuah, J. Kim, Y. Kim, N. Ko, Y. Seo, K. Kim, T.H. Bae, E. Lee, Separation of acetylene from carbon dioxide and ethylene by a water-stable microporous metal-organic framework with aligned imidazolium groups inside the channels, Angew. Chem. Int. Ed. 57 (26) (2018) 7869–7873.

[66] F. Luo, C.S. Yan, L.L. Dang, R. Krishna, W. Zhou, H. Wu, X.L. Dong, Y. Han, T.L. Hu, M. O'Keeffe, L.L. Wang, M.B. Luo, R.B. Lin, B.L. Chen, UTSA-74: A MOF-74 isomer with two accessible binding sites per metal center for highly selective gas separation, J. Am. Chem. Soc. 138 (2016) 5678–5684.

Supporting Information

Collaborative Pore Partition and Pore Surface Fluorination within a Metal-Organic Framework for High-Performance C_2H_2/CO_2 Separation

Xing-Ping Fu,[a,d] Yu-Ling Wang,[a,*] Xue-Feng Zhang,[a] Rajamani Krishna,[c] Chun-Ting He,[a] Qing-Yan Liu,[a,*] and Banglin Chen[b,*]

[a] *College of Chemistry and Chemical Engineering, Key Laboratory of Functional Small Molecules for Ministry of Education, Jiangxi Normal University, Nanchang 330022, Jiangxi, PR China. E-mail: ylwang@jxnu.edu.cn; qyliuchem@jxnu.edu.cn*

[b] *Department of Chemistry, University of Texas at San Antonio One UTSA Circle, San Antonio, TX 78249-0698, USA. E-mail: banglin.chen@utsa.edu*

[c] *Van 't Hoff Institute for Molecular Sciences, University of Amsterdam, Science Park 904, 1098 XH Amsterdam, The Netherlands*

[d] *Department of Ecological and Resources Engineering, Fujian Key Laboratory of Eco-industrial Green Technology, Wuyi University, Wuyishan 354300, Fujian, P. R. China.*

Table S1. Physical parameters for C_2H_2 and CO_2.

	Molecular size /Å^3	Boiling point /K	Kinetic diameter /Å	Polarizability $\times10^{25}$ /cm^3	Quadruple moment $\times10^{26}$ esu/cm^2	Dipole moment /esu cm
C_2H_2	3.32 × 3.34 × 5.7	189.3	3.3	33.3-39.3	3.0	0
CO_2	3.18 × 3.33 × 5.36	194.7	3.3	29.11	4.30	0

General Methods and Materials

All chemicals were obtained from commercial sources and used without further purification except 3,3′,5,5′-tetrakis(fluoro)biphenyl-4,4′-dicarboxylate acid (H_2-TFBPDC), which was prepared according to our reported method.[S1] The powder X-ray diffraction patterns (PXRD) were recorded on a Rigaku DMAX 2500 powder diffractometer at 40 kV and 100 mA using Cu-Kα (λ=1.54056 Å). FT-IR spectrum was recorded from KBr disc on a Perkin-Elmer Spectrum One FT-IR spectrometer ranging from 400 to 4000 cm^{-1}. The C, H and N analyses for compounds were performed on Elementar Perkin-Elmer 2400CHN microanalyzer. Thermogravimetric analyses were performed under a nitrogen atmosphere with a heating rate of 10 °C min^{-1} using a PE Diamond thermogravimetric analyser. Water contact angles were measured on compressed powders with a Dataphysics contact angle meter (OCA15EC).

X-Ray Single Crystal Structure Determinations

Single-crystal X-ray diffraction experiments were carried out with a Rigaku Oxford SuperNova diffractometer equipped with an EOS detector (Mo-Kα radiation, λ = 0.71073 Å). Absorption correction and data reduction were handled with a *CrysAlisPro package*.[S2] The *SHELXT-2015* [S3] and *SHELXL-2018* [S4] were applied to structure solution and refinement. Non-H atoms were refined anisotropically. Hydrogen atoms except for the hydrogen atoms of carboxylic ligands were modelled geometrically and refined with a riding model. The biphenyl-4,4′-dicarboxylic in JXNU-12 and 3,3′,5,5′-tetrakis(fluoro)biphenyl-4,4′-dicarboxylic in JXNU-12(F) are symmetrically disordered with two positions. Hydrogen attached to the disordered carboxylic ligands were not added but included into the formulas. The guest solvent molecules and dimethyl amine cations are highly disordered and treated by *SQUEEZE* of *PLATON*.[S5] Thus the dimethyl amine cations are not included into the formulas. The crystallographic data are provided in Table S2.

Table S2. Crystal structure refinement data.

	JXNU-12	**JXNU-12(F)**
Empirical formula	$C_{60}H_{36}N_6O_{13}Ni_3$	$C_{60}H_{24}F_{12}N_6O_{13}Ni_3$
Formula weight	1225.08	1440.98
Temperature	293(2) K	293(2) K
Wavelength	0.71073 Å	0.71073 Å
Crystal system	hexagonal	hexagonal
space group	$P6_3/mmc$	$P6_3/mmc$
a (Å)	16.7094(2)	16.7401(5)
b (Å)	16.7094(2)	16.7401(5)
c (Å)	25.8026(4)	25.8912(11)
α (°)	90	90
β (°)	90	90
γ (°)	120	120
Volume(Å^3)	6239.16(18)	6283.5(3)
Z	2	2
Calculated density(mg/m^{-3})	0.652	0.762
F (000)	1252.0	1444.0
Limiting indices	-18 <= h <= 17, -13 <= k <= 20, -32 <= l<= 32	-10 <= h <= 19, -20 <= k <= 20, -32 <= l<= 28
Reflections collected	16137	17657
Independent reflections	2404 [R_{int} = 0.0276]	2423 [R_{int} = 0.1256]
Goodness-of-fit on F^2	1.131	1.040
Final R_1 [I>2sigma(I)]	0.0713	0.0724
wR_2 (all data)	0.1971	0.2275
CCDC number	2104433	2104434

Gas Adsorption

Gas sorption-desorption isotherms were measured on a Micromeritics ASAP 2020 HD88 surface-area and pore-size analyzer up to 1 atm of gas pressure by the static volumetric method. N_2 (99.99%), C_2H_2 (99.95%), and CO_2 (99.99%) were purchased and directly used. The Brunauer-Emmett-Teller (BET) surface area and the pore size distribution data was calculated from N_2 adsorption isotherms at 77 K. Before adsorption measurements, the as-synthesized JXNU-12 and JXNU-12(F) were washed with DMF several times, followed by solvent exchange with acetonitrile for 4 days at 50 ℃. Then, the JXNU-12 and JXNU-12(F) were activated under a dynamic vacuum at 110 ℃ and 125 ℃ for 24 h, respectively.

Isosteric Analysis of the Heat of Adsorption

The gas adsorption isotherms measured at 273, 283, and 298 K were first fitted to a virial equation (eqn (1)). Then the Q_{st} values for C_2H_2 and CO_2 were calculated based on the fitting parameters using eqn (2).[S6]

$$\ln P = \ln N + \frac{1}{T}\sum_{i=0}^{m} a_i N^i + \sum_{i=0}^{n} b_i N^i \qquad \text{eqn (1)}$$

$$Q_{st} = -R\sum_{i=0}^{m} a_i N^i \qquad \text{eqn (2)}$$

where P is pressure(mmHg), N is the adsorbed quantity (mmol g^{-1}), T is the temperature (K), a_i and b_i are virial cofficients, R is the universal gas constant (8.314 J K^{-1} mol^{-1}), and m and n determine the number of coefficients required to adequately describe the isotherm.

Ideal adsorbed solution theory (IAST) calculations of adsorption selectivity and uptake capacities

The Ideal adsorbed solution theory (IAST)[S7] was used to predict mixed gas behavior from experimentally measured single-component isotherms. The experimentally measured loadings for C_2H_2 and CO_2 of JXNU-12(F) and JXNU-12(F) at 273, 283, and 298 K were fitted with the single-site Langmuir isotherm model (eqn(3)).

$$q = q_{sat}\frac{bp}{1+bp} \qquad \text{eqn (3)}$$

Where p (unit: kPa) is the pressure of the bulk gas at equilibrium with the adsorbed phase. q (unit: mol kg^{-1}) is the adsorbed amount per mass of adsorbent. q_{sat} (unit: mmol g^{-1}) is the saturation capacity. The Langmuir parameter b is temperature-dependent (eqn(4)).

$$b = b_0 \exp\left(\frac{E}{RT}\right) \qquad \text{eqn (4)}$$

where E is the energy parameter, with units of J mol^{-1}.

The fitted Langmuir parameters are provided in

and **Error! Reference source not found.**.

Table S3. 1-site Langmuir parameter fits for C_2H_2, and CO_2 in JXNU-12(F).

	q_{sat}	b_0	E
	mol kg^{-1}	Pa^{-1}	kJ mol^{-1}
C_2H_2	40	4.71642E-11	24.4
CO_2	18	4.08216E-10	19.3

Table S4. 1-site Langmuir parameter fits for C_2H_2, and CO_2 in JXNU-12.

	q_{sat}	b_0	E
	mol kg^{-1}	Pa^{-1}	kJ mol^{-1}
C_2H_2	30.5	2.40911E-10	22.3
CO_2	22	1.06144E-10	21.7

Finally, the adsorption selectivity is calculated with eqn(4) using the Langmuir fitting parameters.

$$S_{ads} = \frac{q_1/q_2}{y_1/y_2} \qquad \text{eqn (5)}$$

where the q_1, and q_2 represent the molar loadings, expressed in mol kg^{-1}, within the MOF that is in equilibrium with a bulk fluid mixture with mole fractions y_1, and $y_2 = 1 - y_1$. The molar loadings are usually expressed with the unit of mol kg^{-1}. The IAST calculations of 50/50 mixture adsorption taking the mole fractions $y_1 = 0.5$ and $y_2 = 1 - y_1 = 0.5$ for a range of pressures up to 100 kPa and 298 K were performed.

C_2H_2/CO_2 Breakthrough Simulations

Transient breakthrough simulations were carried out for 50/50 C_2H_2/CO_2 mixtures in beds packed with JXNU-12(F) and JXNU-12(F) operating at a total pressure of 1 bar and 298 K, using the methodology described in earlier publications.[S8-S12] For the breakthrough simulations, the following parameter values were used: length of packed bed, L = 0.3 m; voidage of packed bed, ε = 0.4; superficial gas velocity at inlet, u = 0.04 m/s.

The y-axis is the dimensionless concentrations of each component at the exit of the fixed bed, normalized with respect to the inlet feed concentrations. The x-axis is the *dimensionless* time, $\tau = \frac{tu}{L\varepsilon}$, defined by dividing the actual time, t, by the characteristic time, $\frac{L\varepsilon}{u}$.

The separation potential is defined by Krishna[S8,S9] as follows

$$\Delta Q = Q_1 \frac{p_2}{p_1} - Q_2 \qquad \text{eqn (6)}$$

Q_2 and Q_2 represent the gravimetric uptake capacity (mmol g^{-1}) within the MOF that is in equilibrium with a bulk fluid mixture with mole fractions y_1, and $y_2 = 1 - y_1$. For 50/50 C_2H_2/CO_2 mixtures, $p_1 = p_2$ and $y_2 = y_1$, $\Delta Q = Q_1 - Q_2$.

C_2H_2/CO_2 Breakthrough Experiments

The breakthrough experiments for the separation of C_2H_2/CO_2 (v/v, 50/50) were carried out in fixed beds. Activated

crystalline samples JXNU-12(F) (1.1g) or JXNU-12 (0.71 g) were packed into a stainless steel column (inner diameter: 5.0 mm, length: 200 mm) with silica wool filling void space of the steel column. Before breakthrough experiments, the samples were firstly washed with DMF several times, followed by solvent exchange with acetonitrile for 4 days at 50 ℃, then the samples were activated *in situ* in the column at 383 K for JXNU-12 and 398 K for JXNU-12(F) for 24 h under vacuum condition. After that, the columns were first purged with a flow of He (15 mL min^{-1}) for 1 h at 298 K. The flow of He gas was turned off while the mixture of C_2H_2/CO_2 (v/v, 50/50) was then fed into the column. The outlet gases of the breakthrough column were monitored in real time by the gas chromatograph detection system (TCD-Thermal Conductivity Detector). After the first breakthrough experiment, the sample was regenerated by flushing the adsorption bed with a He flow (15 mL min^{-1}) for 1 hour at 298 K. Subsequently, the column was allowed to equilibrate at the measurement rate before we switched the gas flow.

Grand canonical Monte Carlo (GCMC) simulation.

All the grand canonical Monte Carlo (GCMC) simulations were performed by the Materials Studio package. The adsorption sites of C_2H_2 and CO_2 at 273 K were obtained from GCMC simulations through the fixed loading task in the Sorption module. The host framework and the guest molecules were both regarded as rigid. The simulation box consisted of one unit cell and the Metropolis method based on the universal forcefield (UFF) was used. The cutoff radius was chosen as 15.5 Å for the Lennard-Jones potential, and the equilibration steps and production steps were both set as 5×10^6.

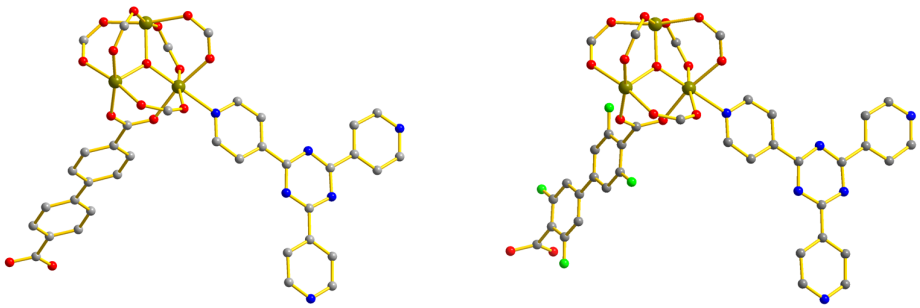

Figure S1 Coordination environments for Ni^{2+} atoms in (a) JXNU-12 and (b) JXNU-12(F) showing the [$Ni_3(\mu_3$-O)] unit.

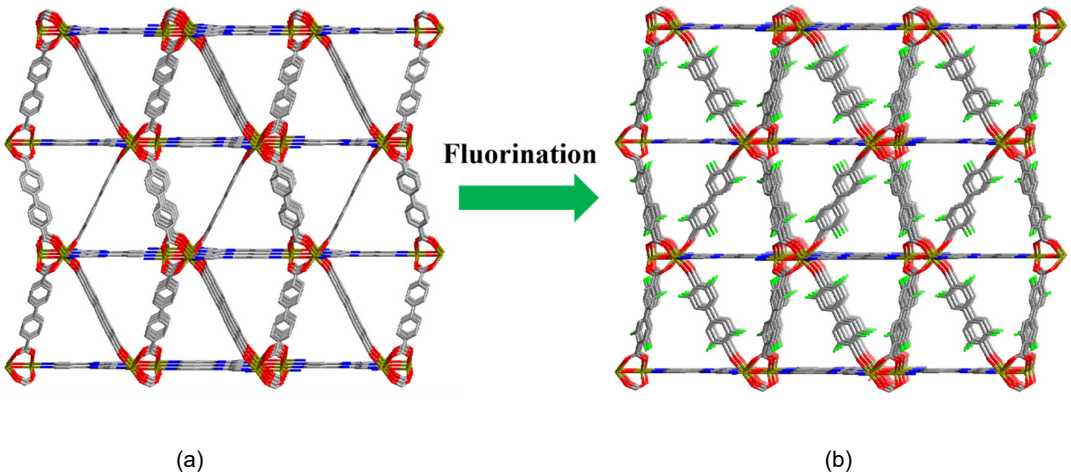

Figure S2 The 3D frameworks for (a) JXNU-12 and (b) JXNU-12(F).

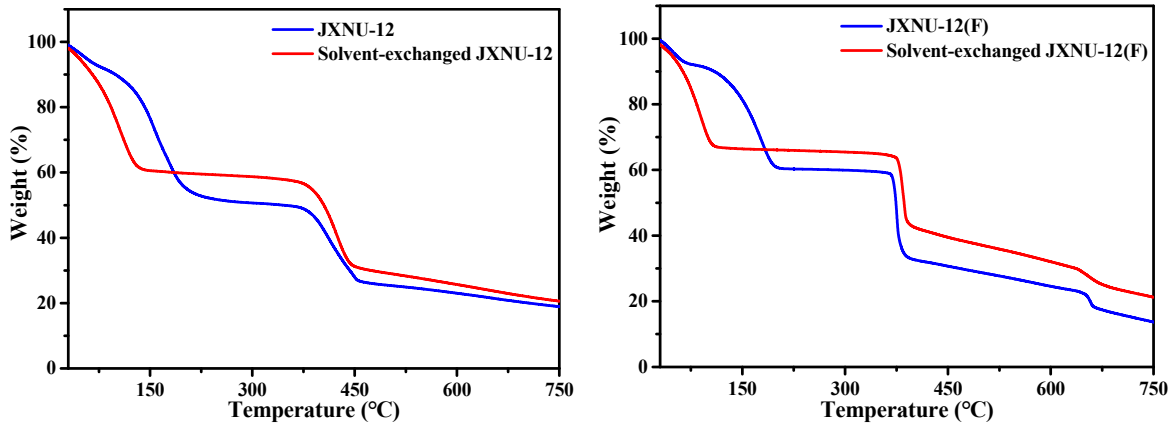

Figure S3 TGA curves for JXNU-12 and JXNU-12(F).

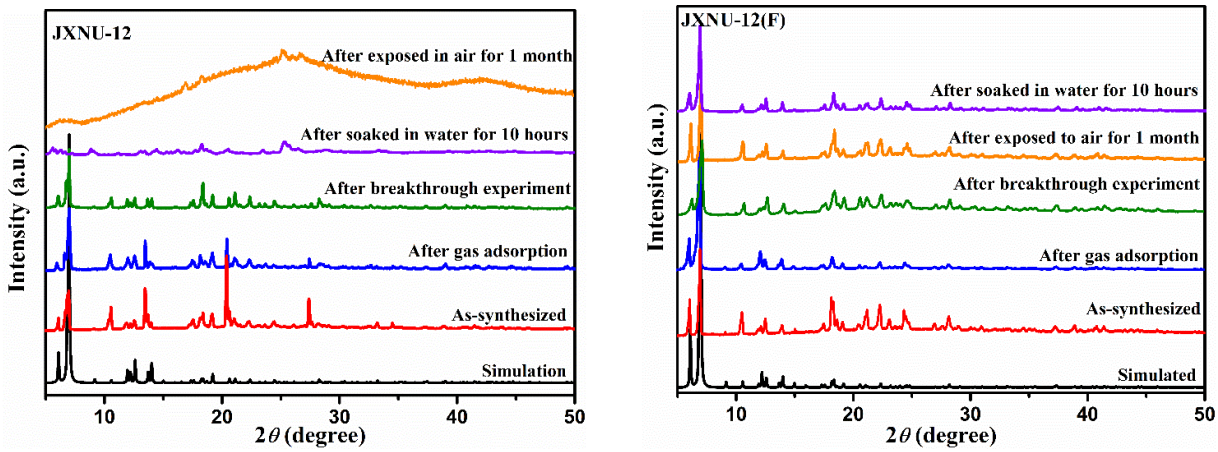

Figure S4 PXRD patterns for JXNU-12 and JXNU-12(F).

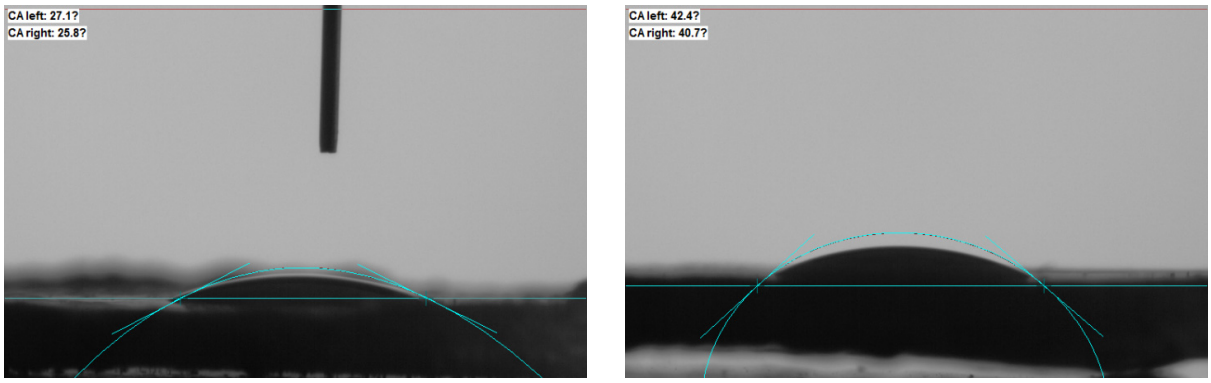

(a) (b)

Figure S5 Photographs for water contact angle measurements for (a) JXNU-12 and (b) JXNU-12(F).

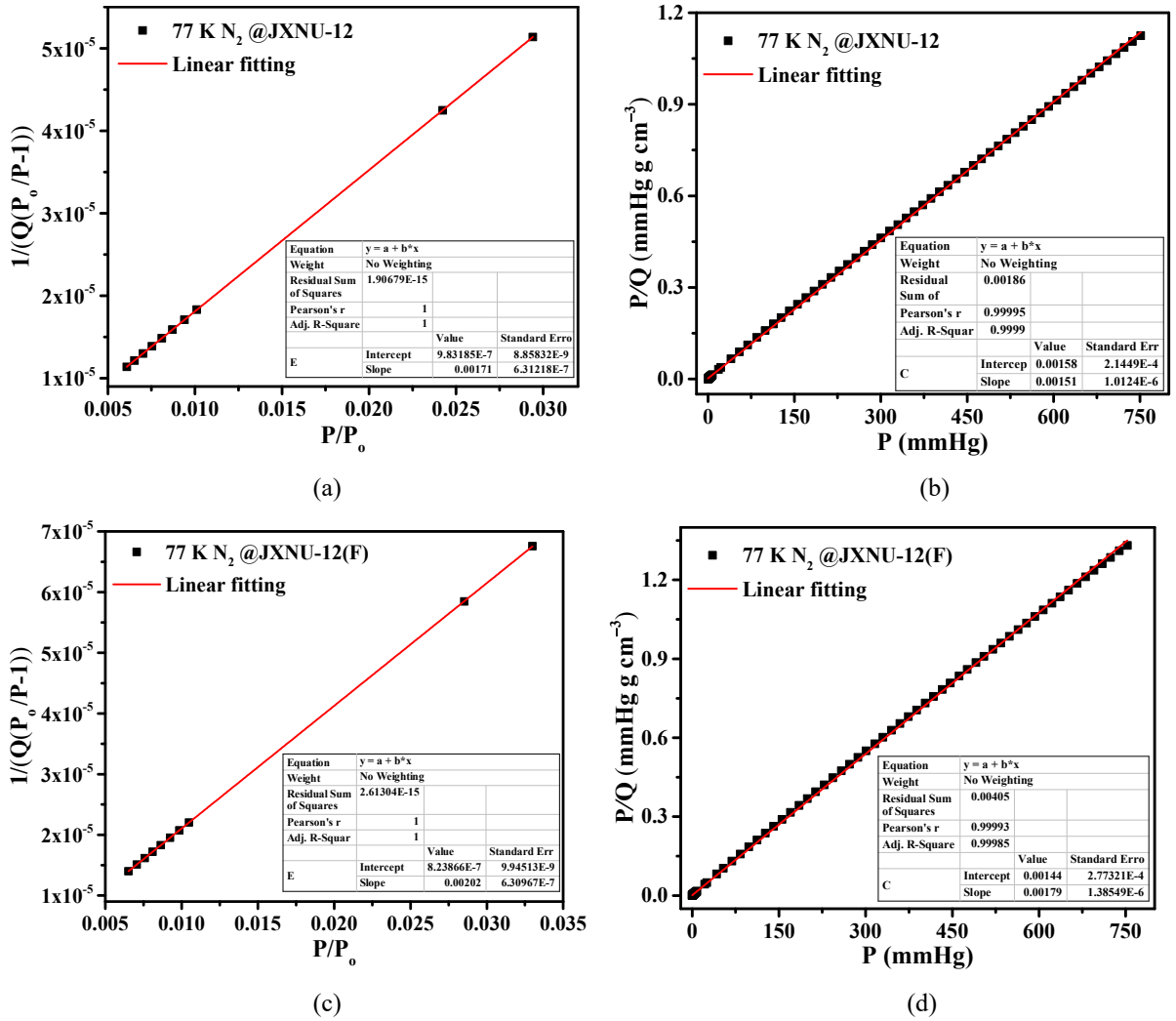

(a) (b)

(c) (d)

Figure S6 (a) and (c) BET surface area plots, and (b) and (d) Langmuir surface area plots.

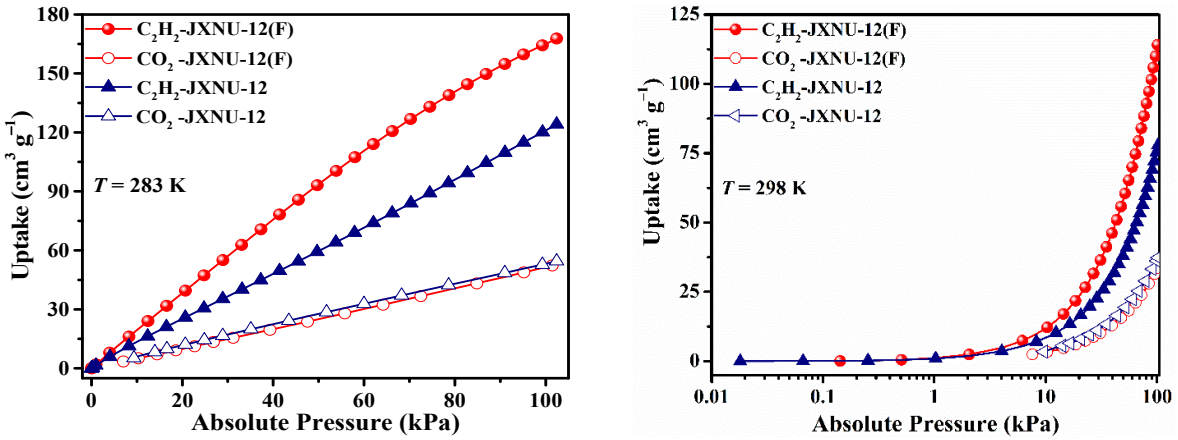

(a) (b)

Figure S7 C_2H_2 and CO_2 adsorption isotherms of JXNU-12 and JXNU-12(F) at 283 and 298 K.

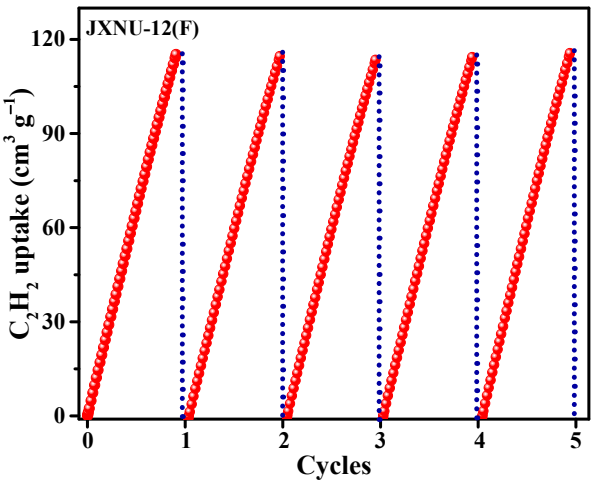

Figure S8 The cyclic C_2H_2 uptake for JXNU-12(F) at 298 K.

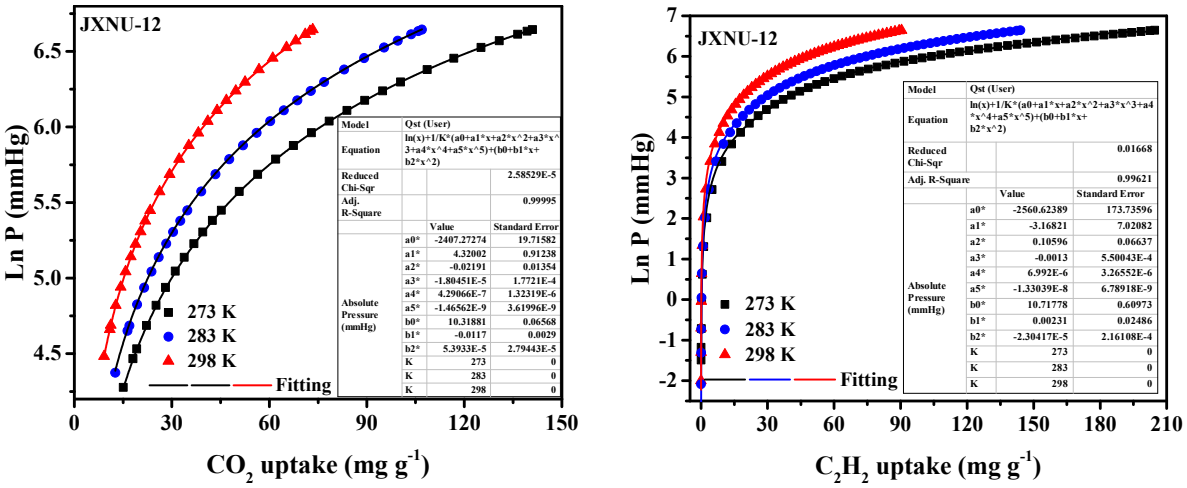

Model	Qst (User)		
Equation	ln(x)+1/K*(a0+a1*x+a2*x^2+a3*x^3+a4*x^4+a5*x^5)+(b0+b1*x+b2*x^2)		
Reduced Chi-Sqr			2.58529E-5
Adj. R-Square			0.99995
		Value	Standard Error
Absolute Pressure (mmHg)	a0*	-2407.27274	19.71582
	a1*	4.32002	0.91238
	a2*	-0.02191	0.01354
	a3*	-1.80451E-5	1.7721E-4
	a4*	4.29066E-7	1.32319E-6
	a5*	-1.46562E-9	3.61996E-9
	b0*	10.31881	0.06568
	b1*	-0.0117	0.0029
	b2*	5.3933E-5	2.79443E-5
	K	273	0
	K	283	0
	K	298	0

Model	Qst (User)		
Equation	ln(x)+1/K*(a0+a1*x+a2*x^2+a3*x^3+a4*x^4+a5*x^5)+(b0+b1*x+b2*x^2)		
Reduced Chi-Sqr			0.01668
Adj. R-Square			0.99621
		Value	Standard Error
Absolute Pressure (mmHg)	a0*	-2560.62389	173.73596
	a1*	-3.16821	7.02082
	a2*	0.10596	0.06637
	a3*	-0.0013	5.50043E-4
	a4*	6.992E-6	3.26552E-6
	a5*	-1.33039E-8	6.78918E-9
	b0*	10.71778	0.60973
	b1*	0.00231	0.02486
	b2*	-2.30417E-5	2.16108E-4
	K	273	0
	K	283	0
	K	298	0

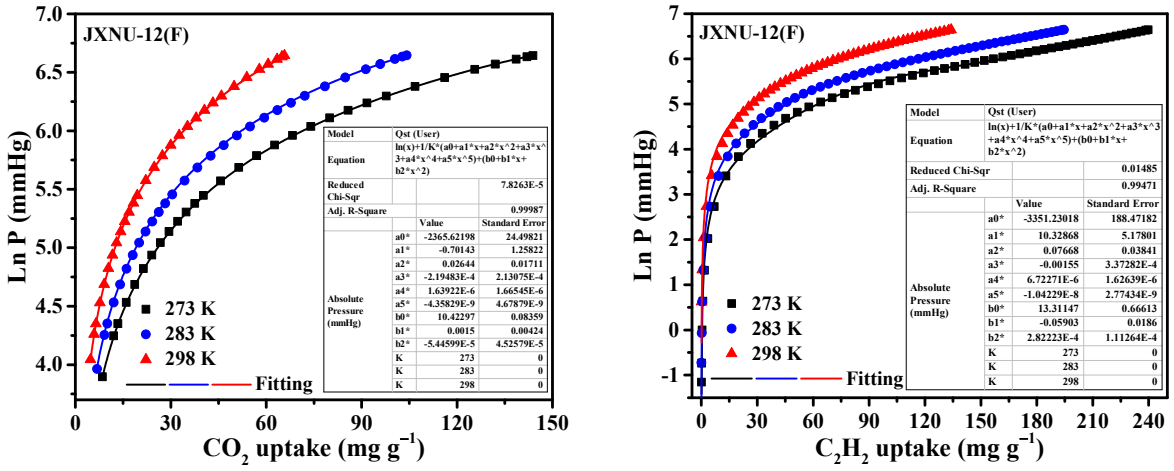

Figure S9 Virial fits of CO_2 and C_2H_2 isotherms for JXNU-12 and JXNU-12(F).

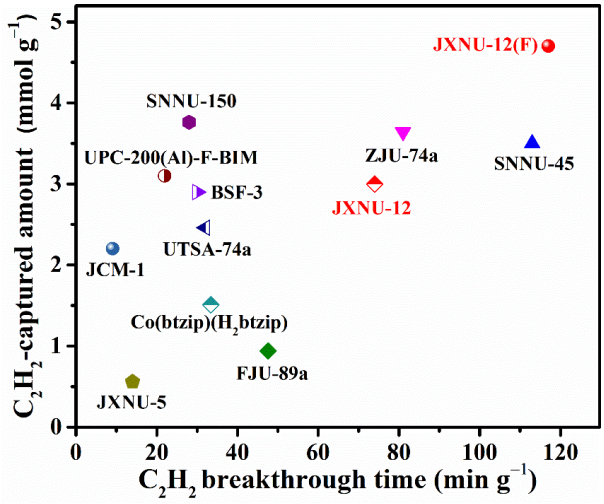

Figure S10 Comparison of MOFs with top-high C_2H_2/CO_2 breakthrough performance at 298 K and 1 bar.

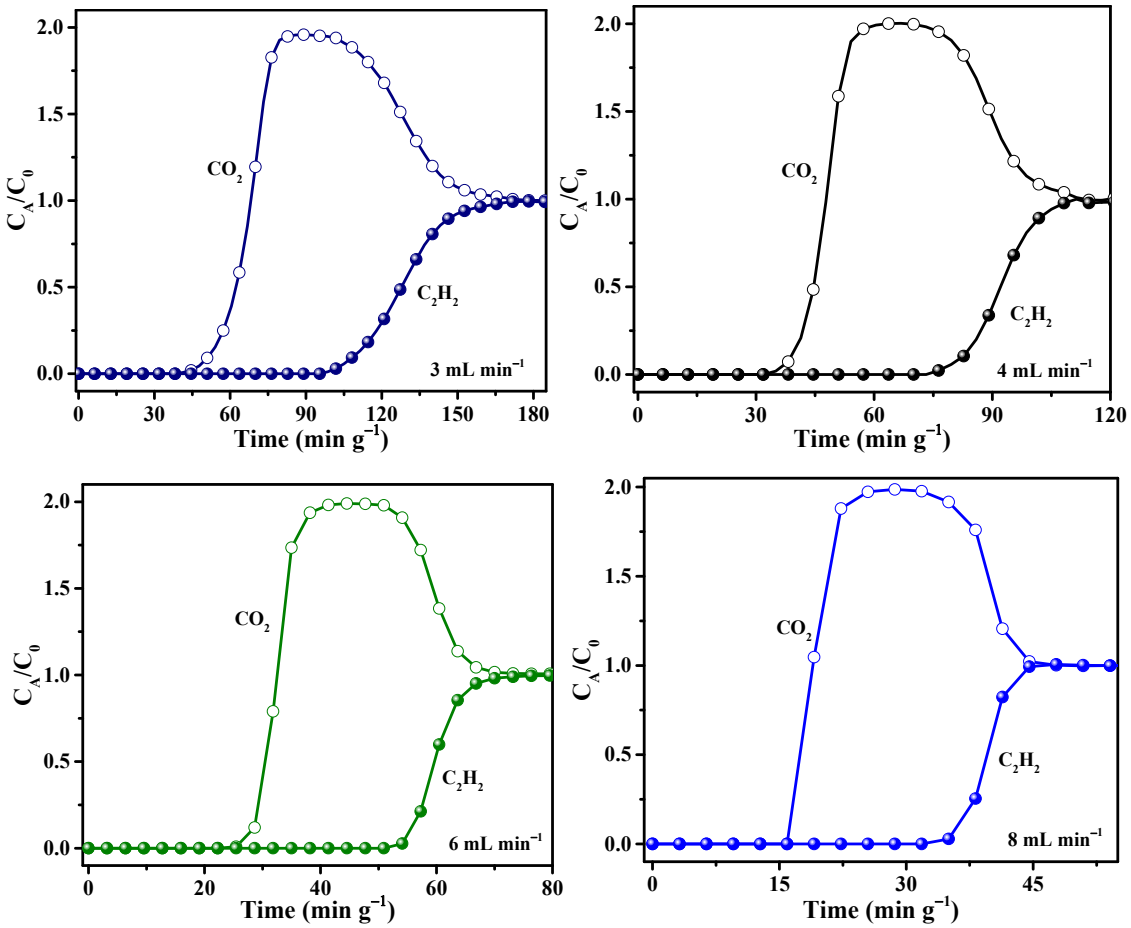

Figure S11 The experimental breakthrough curves of JXNU-12(F) for C_2H_2/CO_2 (v:v=50:50) at different total flow rates (298 K and 1 bar).

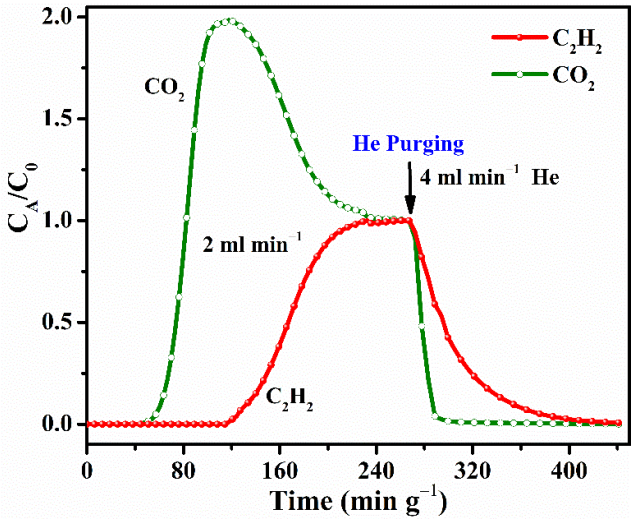

Figure S12 The breakthrough curves and desorption curves for JXNU-12(F) at 298 K and 1 bar.

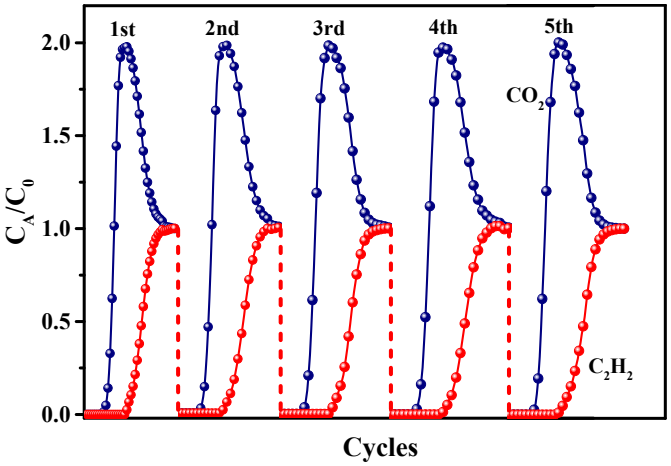

Figure S13 The cycling breakthrough curves for JXNU-12(F) with a total flow rate of 2 ml min^{-1} at 298 K and 1 bar.

References

[1] Z. T. Lin, Q. Y. Liu, L. Yang, C. T. He, L. Li, Y. L. Wang, Fluorinated Biphenyldicarboxylate-Based Metal–Organic Framework Exhibiting Efficient Propyne/Propylene Separation, Inorg. Chem. 59 (2020) 4030–4036.

[2] CrysAlisPro; Rigaku Oxford Diffraction: The Woodlands, TX (2015).

[3] G. M. Sheldrick, SHELXT-integrated space-group and crystalstructure determination, Acta Crystallogr., Sect. A: Found. Adv. A71 (2015) 3–8.

[4] G. M. Sheldrick, Crystal structure efinement with SHELXL. Acta Crystallogr., Sect. C: Struct. Chem. 71 (2015) 3–8.

[5] A. L. Spek, PLATON: A multipurpose Crystallographic Tool; Utrecht University: Utrecht, The Netherlands (2001).

[6] J. L. C. Rowsell, O. -M. Yaghi, Effects of Functionalization, Catenation, and Variation of the Metal Oxide and Organic Linking Units on the Low-Pressure Hydrogen Adsorption Properties of Metal−Organic Frameworks, J. Am. Chem. Soc. 128 (2006) 1304–1315.

[7] A. L, Myers, J. M. Prausnitz, Thermodynamics of Mixed-Gas Adsorption, AIChE J. 11 (1965) 121–127.

[8] R. Krishna, Screening Metal-Organic Frameworks for Mixture Separations in Fixed-Bed Adsorbers using a Combined Selectivity/Capacity Metric, RSC Adv. 7 (2017) 35724–35737.

[9] R. Krishna, Metrics for Evaluation and Screening of Metal-Organic Frameworks for Applications in Mixture Separations, ACS Omega. 5 (2020) 16987−17004.

[10] R. Krishna, The Maxwell-Stefan Description of Mixture Diffusion in Nanoporous Crystalline Materials, Microporous Mesoporous Mater. 185 (2014) 30−50.

[11] R. Krishna, Methodologies for Evaluation of Metal-Organic Frameworks in Separation Applications, RSC Adv. 5 (2015) 52269−52295.

[12] R. Krishna, Methodologies for Screening and Selection of Crystalline Microporous Materials in Mixture Separations, Sep. Purif. Technol. 194 (2018) 281−300.